The effect of defects and disorder on the electronic properties of ZnIr2O4

David Muñoz Ramo and Paul D. Bristowe

Articles you may be interested in

Strain tuning of native defect populations: The case of Cu2ZnSn(S,Se)4
APL Mat. 2, 012110 (2014); 10.1063/1.4863076

Calculated properties of point native defects and p-type conductivity of ZnRh2O4
J. Appl. Phys. 114, 033711 (2013); 10.1063/1.4816000

Chemical effect of Si+ ions on the implantation-induced defects in ZnO studied by a slow positron beam
J. Appl. Phys. 113, 043506 (2013); 10.1063/1.4789010

Effect of Li-doping on the magnetic properties of ZnO with Zn vacancies
J. Appl. Phys. 111, 093902 (2012); 10.1063/1.4707888

Room-temperature ferromagnetism in epitaxial Mg-doped SnO2 thin films
Appl. Phys. Lett. 100, 182405 (2012); 10.1063/1.4711220

The effect of defects and disorder on the electronic properties of ZnIr$_2$O$_4$

David Muñoz Ramo[a)] and Paul D. Bristowe[b)]
Department of Materials Science and Metallurgy, University of Cambridge, 27 Charles Babbage Road,
Cambridge CB3 0FS, United Kingdom

We analyze by means of *ab initio* calculations the role of imperfections on the electronic structure of ZnIr$_2$O$_4$, ranging from point defects in the spinel phase to the fully amorphous phase. We find that interstitial defects and anion vacancies in the spinel have large formation energies, in agreement with the trends observed in other spinels. In contrast, cation vacancies and antisites have lower formation energies. Among them, the zinc antisite and the zinc vacancy are the defects with the lowest formation energy. They are found to act as acceptors, and may be responsible for the spontaneous hole doping in the material. They may also induce optical transitions that would reduce the transparency of the material. Amorphization of ZnIr$_2$O$_4$ leads a large decrease of the band gap and appearance of localized states at the edges of the band gap region, which may act as charge traps and prevent amorphous ZnIr$_2$O$_4$ from being a good hole conductor. © *2014 AIP Publishing LLC.*
[http://dx.doi.org/10.1063/1.4893556]

I. INTRODUCTION

The search for transparent conducting oxides suitable for technological applications has yielded over the years many interesting materials for use in the field of optoelectronics, like transparent conducting layers for solar cells, light emitting diodes and transparent electronic devices, among other applications.[1–3] The area of *n*-type oxides is well developed, with materials like indium tin oxide, indium zinc oxide, or other doped phases of ZnO that display a good combination of transparency and electron conductivity, both in the crystal and the amorphous phases. However, progress has been slower in the development of good *p*-type transparent conducting oxides. The inversion of common *n*-type oxides to *p*-type conductivity by doping has proven to be extremely difficult and the resulting materials display poor conductivities.[4,5] This is due to the nature of the valence band in these materials, which is composed of narrow oxygen *p* bands that lead to high effective masses for the holes and poor carrier conductivities. Alternative approaches have appeared over the years, in which the valence band is engineered by substituting the oxygen *p* band in the gap region for that of another element. The first successful attempts were made with delafossites based on CuAlO$_2$.[6] In these materials, the top of the valence band is composed of *d* states of Cu hybridized with *p* states of oxygen. However, although these materials are transparent, hole conductivities in the amorphous phase have proved to be too small for optoelectronic applications.[7]

More recently, oxides in the spinel structure with zinc and transition metals with a *d*^{6} closed shell configuration have been studied. In this structure, the Zn atoms are bonded to four O atoms in a tetrahedral environment and the *d*^{6} transition metals have a coordination environment of six O atoms with octahedral symmetry. The transparent spinel ZnRh$_2$O$_4$ was

reported to have *p*-type conductivity with no intentional doping and a band gap of around 2.1–2.7 eV.[8] The transparency of ZnRh$_2$O$_4$ is a consequence of the octahedral environment of the Rh atoms, which produces a splitting of the *d* levels into a fully occupied t_{2g}^6 band and an empty e_g^0 band and opens a band gap in the material. Recently, an oxide composed of zinc and iridium with the same spinel structure has been produced in thin films,[9,10] with promising values for both transparency (band gap of around 3.0 eV) and hole conductivity (2–3 S cm^{-1}). In a similar way to ZnRh$_2$O$_4$, the band gap is created by the t_{2g}^6 - e_g^0 splitting of the Ir *d* bands in an octahedral environment. Unintentional *p*-type conductivity is also present, probably caused by the presence of defects in the structure that introduce holes in the material. *Ab initio* calculations on several spinels[11,12] suggest cation nonstoichiometry as the most probable source of holes, although further study is required for the particular case of ZnIr$_2$O$_4$ to determine the defects responsible for this behaviour. In addition, information about the amorphous phase would be helpful, as this phase is preferred in technological applications for its better homogeneity and absence of grain boundaries. The key question in this case is whether the properties that make the spinel phase interesting (good *p*-type conductivity, transparency) are conserved after amorphization. Computer modelling using state-of-the-art methods can provide useful insight into this question.

In this work, we use density functional theory to study the stability and properties of common point defects in ZnIr$_2$O$_4$, namely, cation and anion vacancies and interstitials, and cation antisites. Then, we construct a model for the amorphous phase using molecular dynamics and classical interatomic potentials and determine its geometrical features and its electronic structure using density functional theory on a representative subset of the resulting structure. We present the *ab initio* method used in Sec. II. In Sec. III, we describe the main features and stability region of the spinel ZnIr$_2$O$_4$, followed by a study of the defect formation

a)Electronic mail: dm586@cam.ac.uk
b)Electronic mail: pdb1000@cam.ac.uk

141, 084704-1

energies in Sec. IV and a discussion of the crystalline and electronic structure of the defects with the lowest formation energies in Sec. V. Then, we describe the geometry and electronic structure of our model for the amorphous phase in Sec. VI. Finally, we discuss the impact of the presence of defects and the amorphization of $ZnIr_2O_4$ on the properties of technological interest before giving our conclusions.

II. COMPUTATIONAL METHOD

A. *Ab initio* calculations

The periodic density functional theory calculations were performed with the CRYSTAL09 package,[13] which uses local basis sets of Gaussian-type orbitals, and the hybrid B3LYP functional in order to obtain a good estimate of the band gap of $ZnIr_2O_4$. This functional has been used to predict defect properties and charge localization phenomena in previous studies of $ZnIr_2O_4$,[14] and in oxides like hexagonal ZnO,[15–17] monoclinic HfO_2,[18] crystalline and amorphous SiO_2,[19,20] and in many other oxides.[21,22] We omitted spin-orbit coupling effects as they only have a minor effect on the band structure of bulk $ZnIr_2O_4$.[23] We considered a 112-atom supercell for the defect calculations in the crystal phase, as defect calculations on similar spinel oxides show that this size is sufficient to obtain accurate results.[12] Charged defects were studied with a compensating charge background. For the amorphous phase, a 91-atom supercell was found to be large enough to represent the general features of this phase.

B. Calculation of the formation energies

Formation energies H_q for the different defects in the $ZnIr_2O_4$ structure were calculated using the following expression:

$$H_q(E_F, \mu) = (E_q - E_H) + q(E_V + \Delta E_F)$$
$$+ \sum_\alpha n_\alpha(\mu_\alpha^0 + \Delta\mu_\alpha). \quad (1)$$

E_q is the total energy of the defect supercell with charge q and E_H is the energy of the perfect supercell. E_V is the valence-band edge energy, ΔE_F is the Fermi energy referred to the valence-band edge, n_α is the number of atoms of species α, μ_α^0 is the standard chemical potential for atom α, and $\Delta\mu_\alpha$ is the relative chemical potential dependent on the conditions of the system.

To calculate the range of $\Delta\mu_\alpha$ for each atom, we take several conditions into account. First, the maximum chemical potential for each element must be the energy of the bulk, therefore $\Delta\mu_\alpha$ must be equal to or smaller than zero for each one of them. We also write equations for the equilibrium between the elemental phases and $ZnIr_2O_4$, and similar expressions for the equilibrium with the binary oxides,

$$\Delta\mu_{Zn} + 2\Delta\mu_{Ir} + 4\Delta\mu_O = \Delta H_f(ZnIr_2O_4), \quad (2)$$

$$\Delta\mu_{Zn} + \Delta\mu_O \le \Delta H_f(ZnO), \quad (3)$$

$$\Delta\mu_{Ir} + 2\Delta\mu_O \le \Delta H_f(IrO_2), \quad (4)$$

$$2\Delta\mu_{Ir} + 3\Delta\mu_O \le \Delta H_f(Ir_2O_3), \quad (5)$$

where the different $\Delta H_f(i)$ correspond to the formation enthalpies (per formula unit) of $ZnIr_2O_4$, ZnO, IrO_2, and Ir_2O_3. We calculate the $\Delta H_f(i)$ as the total energy difference between the oxide and its constituent elements in the bulk. μ_O^0 is calculated as half the energy of a O_2 molecule in a spin polarized calculation. μ_{Zn}^0 and μ_{Ir}^0 would be calculated from the energy of their respective solid phases in a similar manner to μ_O^0. However, B3LYP is well known for providing inaccurate estimates for the energy of metals.[24] To correct this problem, we follow Ahmad *et al.*[25] and calculate corrected values for these chemical potentials by taking the experimental values for $\Delta H_f(IrO_2)$ and $\Delta H_f(ZnO)$, and deducing the correct values for the energy per atom of Zn metal E(Zn) and Ir metal E(Ir) from the equations,

$$\Delta H_f(IrO_2) = E(IrO_2) - E(O_2) - E(Ir), \quad (6)$$

$$\Delta H_f(ZnO) = E(ZnO) - 1/2E(O_2) - E(Zn), \quad (7)$$

where $E(IrO_2)$, $E(ZnO)$, and $E(O_2)$ are the B3LYP energies of the different phases involved.

Additional corrections are incorporated into the calculation of charged defect energies to take into account different effects. We apply a potential alignment correction,[26] which we obtain by aligning the 1s core level of oxygen in the defect supercell to the level in the ideal supercell. We also apply the Makov-Payne correction to electrostatic interaction between defect images in the periodic approach,[27]

$$\Delta E_{MP} = (1 + f)\frac{q^2\alpha_M}{2\epsilon L}. \quad (8)$$

In this expression, α_M is the Madelung constant for the supercell, calculated using the method described in Ref. 28. ϵ is the static dielectric constant; it has been obtained from a phonon calculation in the unit cell of $ZnIr_2O_4$ assuming an average value of 6.0 for the high-frequency part of the dielectric constant, which is a good approximation for most oxides.[29] We obtain a value of 9.38 with the B3LYP functional. L is the average distance between defect images and f is a proportionality factor accounting for the L^{-3} term, which is -0.35 according to Lany and Zunger.[26] The contributions obtained from these corrections range between about 0.1 eV for $+1/-1$ defects and 1.2 eV for $+3/-3$ defects. These values are significant enough to stabilize some charge states over the others in most of the defects considered, and therefore we consider them essential for an accurate description of the formation energies.

Transition levels $\epsilon(q/q')$ determine the energies at which defects change their charge state. Here, we calculate thermodynamic transition levels, where the geometries of the defect at the different charge states are fully relaxed. They may be obtained experimentally using spectroscopic techniques where the final charge state of the defect has enough time to relax to the equilibrium geometry, as in deep-level transient-spectroscopy. They are calculated as the value of the Fermi

level at which charge states q and q' have equal formation energy, using the expression

$$\epsilon(q/q') = \frac{E_{q'} - E_q}{q - q'} - E_v. \tag{9}$$

C. Amorphous phase setup

In order to create a model of the amorphous phases of the Ir spinel, we performed molecular dynamics (MD) simulations using classical interatomic potentials of the Buckingham form for the Ir-O interaction, the Zn-O interaction, and the O-O interaction. These simulations were performed with the DLPOLY code.[30] A rapid quench from the molten state was simulated to obtain the amorphous phase on a cubic supercell of $ZnIr_2O_4$ with 12096 atoms. Further details of the interatomic potentials used and the MD setup can be found in the supplementary material.[31]

The MD model is too large for *ab initio* calculations and therefore we perform the following procedure. A cubic sub-cell is extracted from the large amorphous MD model resulting from the melt-quench process. This cube is taken from the centre of the MD cell and contains about 90 atoms but does not have the exact composition of the parent MD cell. Therefore, atoms are added and removed at random positions in order to match the Ir/Zn/O proportions to those of the MD cell. The sub-cell resulting from this process contains several structural artefacts; the periodic boundaries introduced with the sub-cell are not chosen to preserve the local amorphous structure at the cell faces. Likewise, the random addition/removal of atoms from the cell is performed without any structural consideration. Here, we use the Reverse Monte Carlo technique to remove these structural artefacts and generate a configuration structurally consistent with the large MD cell. This algorithm proceeds in the following way: a sequence of random atom moves are performed on the initial sub-cell with the required composition and density. Each move is accepted or rejected based on whether it improves the fit between the model's partial radial distribution functions and those of the MD simulation. A detailed description of this algorithm can be found in previous studies of liquid, disordered, and amorphous systems.[17,32–34] The resulting structure is further refined by performing geometry optimization, first with the classical potential model described previously and then with the B3LYP functional.

III. PROPERTIES OF BULK ZnIr₂O₄

We proceed to describe the main features of the crystal and electronic structure of the spinel phase of $ZnIr_2O_4$, as well as the range of chemical potentials for which this phase is stable.

A. Electronic and crystalline structure

The crystal structure of $ZnIr_2O_4$ is that of a normal spinel, consisting of a face-centered O lattice with Zn^{2+} and Ir^{3+} ions sitting on tetrahedral and octahedral positions, respectively (see Figure 1). Each O atom is linked to three Ir atoms
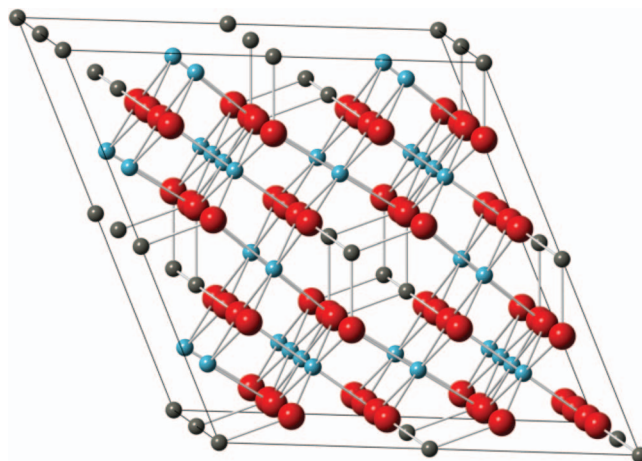

FIG. 1. Scheme of the 112-atom supercell (16 formula units of $ZnIr_2O_4$) used for the *ab initio* calculations. Colors represent the different types of atom present in the structure. Red: O; dark grey: Zn; blue: Ir.

along the $\langle 100 \rangle$ directions and one Zn atom in the $\langle 111 \rangle$ direction with similar bond lengths. The structure has several vacant tetrahedral and octahedral interstices where additional atoms may be accommodated.

Table I compares the parameters calculated with the B3LYP functional and other functionals with the experimental values. The B3LYP lattice parameter is in good agreement with the experimental value and the values obtained with other functionals. B3LYP also predicts a band gap similar to the experimental value obtained by Dekkers *et al.*[9] and slightly larger than the value obtained from other functionals. Figure 2 shows the B3LYP Density of States (DOS) of bulk $ZnIr_2O_4$. The top of the valence band is dominated by a Ir $5d$ band hybridized with O $2p$ states. Below this band sits the O $2p$ band, and the bottom of the valence band is dominated by Zn $3d$ states. The lower conduction band region is mostly composed of $5d$ states of Ir. These features are similar to those found for the spinels $ZnRh_2O_4$ and $ZnCo_2O_4$.[9] There are also some remarkable differences: $ZnIr_2O_4$ has a direct band gap while the gap in $ZnRh_2O_4$ and $ZnCo_2O_4$ is indirect, and the band at the conduction band minimum (CBM) of the Ir spinel is mainly composed of Ir $6s$ and Zn $4s$ states, while in the other two spinels it is mainly composed of the d states of the transition metal. These features are in agreement with theoretical calculations using the HSE functional.[35]

B. Phase stability of ZnIr₂O₄

As described in Sec. II B, we proceed to calculate the chemical potential intervals of stability for $ZnIr_2O_4$. First, we calculate corrected formation enthalpies for $ZnIr_2O_4$ and

TABLE I. Comparison between band gaps and lattice parameters obtained for $ZnIr_2O_4$ with B3LYP, other functionals and experimental data.

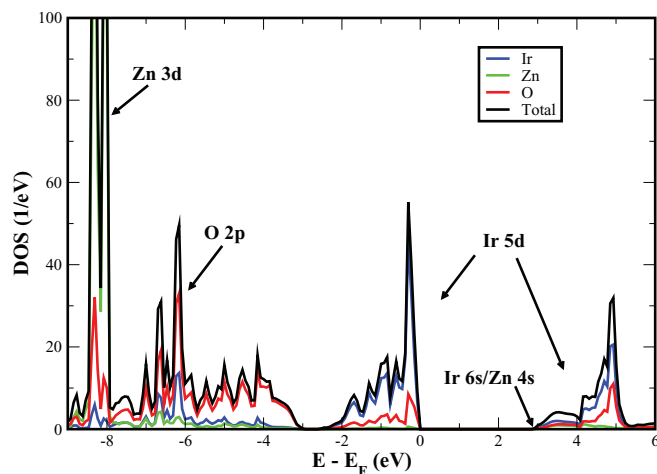|	B3LYP	PBE	HSE	mBJLDA	Expt.
Band gap (eV)	3.06	0.48[35]	2.45[35]	2.25[23]	2.97[9]
a(Å)	8.77	8.75[35]	8.59[35]	...	8.51[9]

FIG. 2. Total and partial Densities of States of bulk $ZnIr_2O_4$ calculated with the B3LYP functional, aligned to the Fermi energy of the material.

FIG. 3. Phase stability diagram of $ZnIr_2O_4$ with respect to elemental O, Zn, and Ir. The Ir-poor, Zn-poor, and O-poor conditions that define the boundaries of the stability region of $ZnIr_2O_4$ have been explicitly marked in the diagram. The region between dashed lines labelled "Exp." corresponds to the range of conditions at which thin films of $ZnIr_2O_4$ were grown in Ref. 9.

Ir_2O_3. $\Delta H_f(IrO_2)$ and $\Delta H_f(ZnO)$ have experimental values of -2.58 eV[36] and -3.76 eV,[37] respectively. With these values, we obtain corrected energies for elementary Zn and Ir and calculate values of -7.02 eV and -2.96 eV for $\Delta H_f(ZnIr_2O_4)$ and $\Delta H_f(ZnIr_2O_4)$, respectively. Inspection of the formation enthalpies for all oxides shows that IrO_2 is more stable than Ir_2O_3, in agreement with experiment.[38] We also observe that $ZnIr_2O_4$ is thermodynamically unstable against decomposition into IrO_2 and ZnO. We have checked this result by recalculating all formation enthalpies and chemical potentials with the PBE functional,[39] and we have obtained the same instability. Other calculations using the HSE functional find a similar conclusion.[12] This result may explain why synthesis of the Ir spinel is so difficult and has been only obtained in thin films, probably as a metastable phase.[9] Despite this, calculation of the formation energy of representative defects in bulk $ZnIr_2O_4$ may give an indication of the relative concentration of defects in the thin film. Therefore, we use the limits imposed by the pure element phases to draw our diagram of allowed chemical potentials from these data, shown in Figure 3. In this diagram, the region of stability of $ZnIr_2O_4$ is delimited by the points corresponding to the O-poor, Zn-poor, and Ir-poor limits, respectively.

IV. DEFECT FORMATION ENERGIES

Using the procedure outlined in Sec. II, we calculated the formation energy of the different defects considered in several charge states. Our results are shown in the diagrams of Figure 4. Inspection of the diagrams at low values of E_F shows that the Zn antisite is the lowest energy defect at O-poor and Ir-poor conditions, and creation of this defect is favored due to the negative values of its formation energy. It only becomes destabilized with respect to other defects when considering Zn-poor conditions. The Ir vacancy also has low formation energy: its creation is favored in Ir-poor conditions and its formation energy becomes about 2.3 eV in O-poor and Zn-poor conditions. On the other hand, the stability of the Zn vacancy and the Ir antisite strongly depend on the growth conditions. In the former case, the formation energy in O-poor and Ir-poor
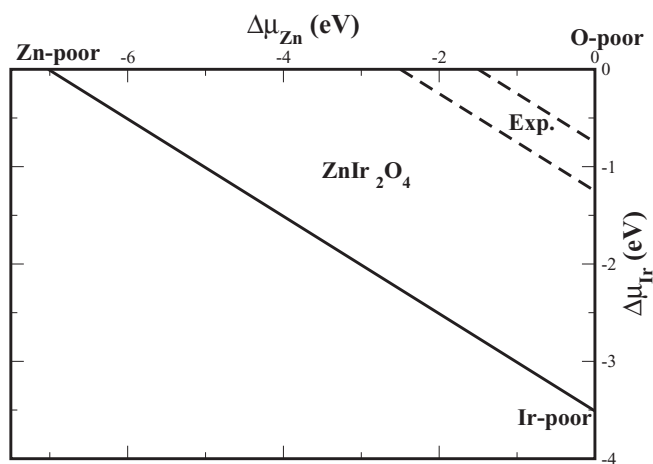
conditions is remarkably high, about 4 eV and is reduced to about -2.4 eV at Zn-poor conditions. In the Ir antisite case, the formation energy varies from about 7.4 eV (Ir-poor) to about -3.3 eV (Zn-poor). The O-related defect formation energies vary in a narrower range, between about 2 eV and 4 eV. The cation interstitials generally have large formation energies, varying between 4.9 eV and 8.4 eV in the Ir case and between 2.3 and 9.5 eV in the Zn case. These results follow trends observed in other spinels,[11] namely, that the cation sublattice is more rigid than the oxygen sublattice, and the large size of the Zn and Ir atoms prevents them from being easily accommodated at interstitial positions. The neutral charge state is the most stable one in the cation and anion vacancies, the O interstitial and the Zn antisite. In contrast, the Ir antisite is stabilized in the $+1$ charge state, and the cation interstitials prefer the $+2$ charge state.

Increasing the value of E_F leads to a decrease in the formation energy and stabilization of negative charge states for the cation vacancies and the Zn antisite. The Ir antisite formation energy increases at first with respect to E_F, then decreases again along with the stabilization of negative charge states. The O vacancy and interstitial are insensitive to the value of E_F. In the case of the cation interstitials, the formation energy increases until reaching a maximum and then becomes fixed and the neutral charge state is stabilized.

The values discussed above have been obtained at extrema with respect to chemical potential on the region of stability of $ZnIr_2O_4$ (Fig. 3). However, one may wonder whether any of these points are representative of the conditions found in the actual synthesis of $ZnIr_2O_4$. The thin films described in Ref. 9 are grown at temperatures between 773 and 973 K and O_2 partial pressure of about 0.250 mbar. Using the procedure outlined in Ref. 40, we can relate the oxygen partial pressure and chemical potential. The area in the phase stability diagram corresponding to these conditions has been marked in Figure 3. We observe that the closest point to this area is the O-poor corner of the diagram, so the most likely defect to be
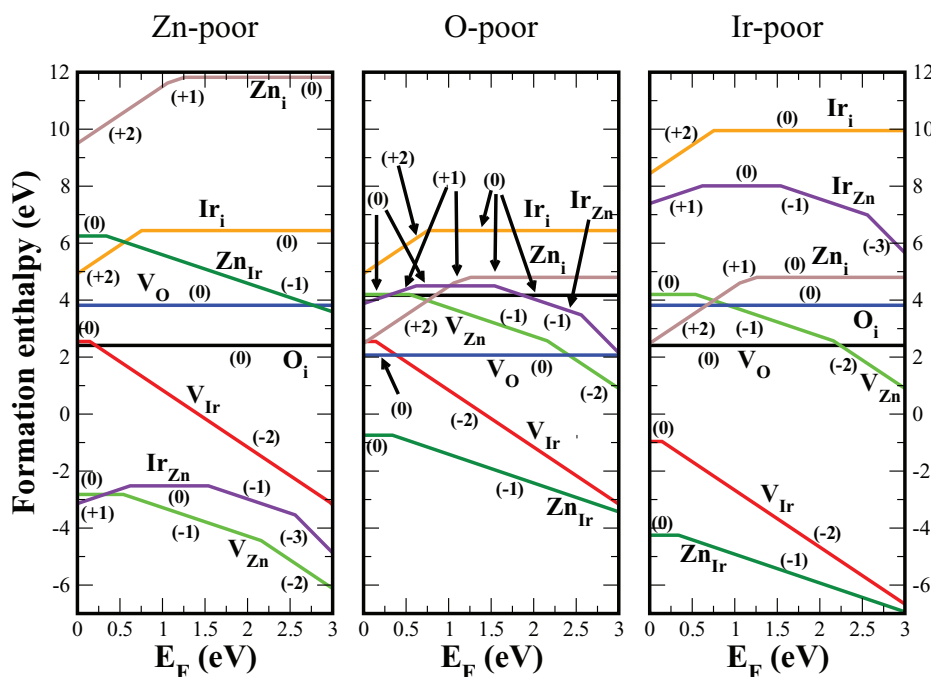
FIG. 4. Formation energies vs. Fermi level for all defects considered in this study in different chemical conditions. Numbers in brackets indicate the charge state at different Fermi energies for each defect.

found is the Zn antisite, and probably the Zn vacancy. The Ir and O vacancies and the Ir antisite may also be present in small quantities.

These results show some agreement with calculations performed using the HSE hybrid functional,[12] regarding the presence of the cation vacancies and Zn antisite at different points on the phase stability diagram, although our results suggest that the Ir antisite may also be present in $ZnIr_2O_4$ for Zn-poor conditions. However, the main difference is found in the charge state of these defects: our calculations predict the neutral state to be the most stable one at low values of E_F for the cation vacancies and the Zn antisite, while the HSE calculations of Ref. 12 favor negative charges for these defects. We believe that the main difference between these results is the inclusion of the Makov-Payne correction to the energies of the charged defects in our calculations, which push their energies to higher values and destabilize them with respect to the neutral state at low values of E_F. Differences in the treatment of the exchange-correlation between B3LYP and HSE may also have some effect although it is thought to be minimal since both hybrid functionals contain approximately the same amount of Hartree-Fock exchange (20%–25%).

V. STRUCTURAL AND ELECTRONIC PROPERTIES OF DEFECTS IN ZnIr₂O₄

In Subsections V A-V E, we describe the B3LYP results for the geometry and electronic structure of defects in $ZnIr_2O_4$ at different charge states. We focus specially on the defects with the lowest formation energy at ambient conditions: the Zn vacancy and the Zn antisite. The Ir vacancy, Ir antisite, and O vacancy are also described, although in less detail. Regarding the interstitial defects, our calculations pre-

dict them to have high formation energies, rendering them unlikely to appear in the spinel structure. Their structural and electronic properties may be found in the supplementary material (Ref. 31).

A. Zn vacancy

The neutral Zn vacancy induces a general displacement of the four nearest neighbour (NN) O atoms away from the cavity. Two O atoms accommodate a localized hole and move about 0.25 Å away, while the other two O atoms move about 0.2 Å away. The local distortion induced by the defect has been represented in Figure 5.

Two doubly occupied acceptor levels are created at about 0.4 eV above the valence band maximum (VBM), as well as a doubly unoccupied level at about 1.0 eV (see Figure 6). These levels are mostly composed of d states corresponding to the NN Ir atoms surrounding the vacancy, with a smaller contribution of p states from the NN O atoms. Addition of up to
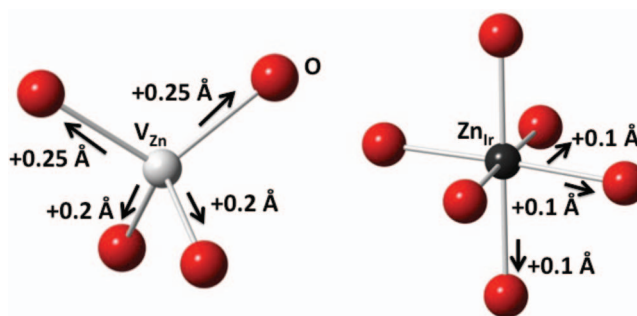

FIG. 5. Details of the structure of the Zn vacancy (left) and Zn antisite (right) in the neutral charge state. Displacements in the local environment around the defect have been represented with arrows displaying the magnitude of the displacement.The color scheme is the same as in Figure 1
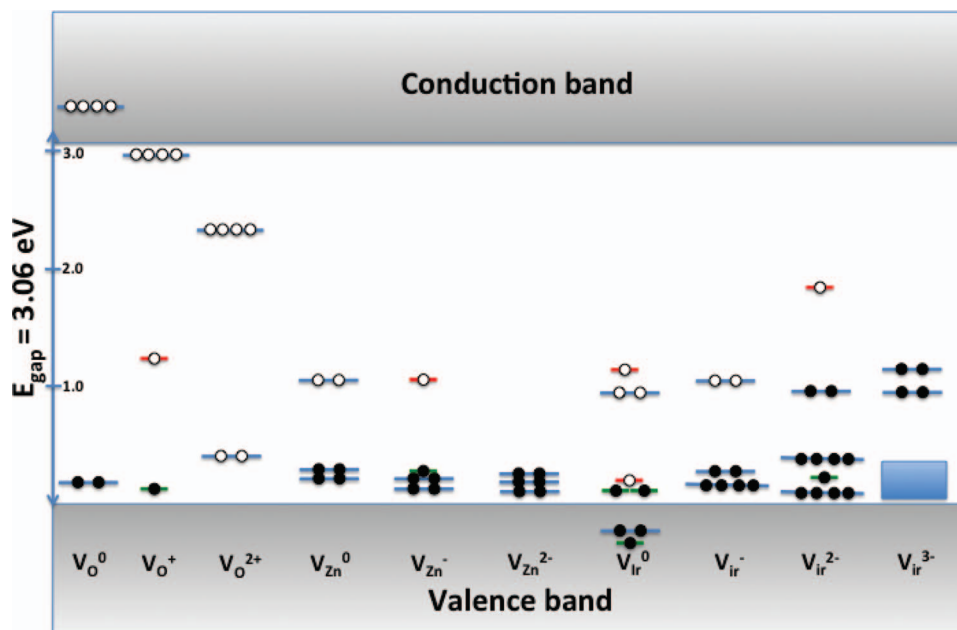
FIG. 6. Diagram representing the gap region of $ZnIr_2O_4$ with the localized states induced by vacancy defects at different charge states. V_X refers to the vacancy (X = Ir, Zn, O). Filled circles represent electrons and open circles represent holes. Levels occupied with only one electron or hole are represented with green lines (spin-up) or red lines (spin-down). The colored box in V_{Ir}^{3-} represents the large group of states induced by the defect.

two electrons to the supercell gradually eliminates the holes located at the two NN O atoms, reduces the O-vacancy distance to match the value of the other two O atoms, and pushes the previously unoccupied levels in the gap down to the top of the VBM.

B. Zn antisite

The neutral Zn antisite slightly modifies the octahedral symmetry of the Ir site in the perfect system, with only three

cation-oxygen bonds maintaining the original length and the other three increasing by about a 5%, as shown in Figure 5. The Zn atom in the antisite largely remains as a +2 ion, and the additional hole is distributed between three NN Ir atoms and two NN O atoms. One double occupied and one single occupied localized level with contributions of the d states from the NN Ir atoms and p states from the NN O atoms are formed at 0.3 eV above the VBM and one spin-down unoccupied level is formed at about 1 eV from the VBM (see Figure 7). In addition, three doubly occupied resonant d
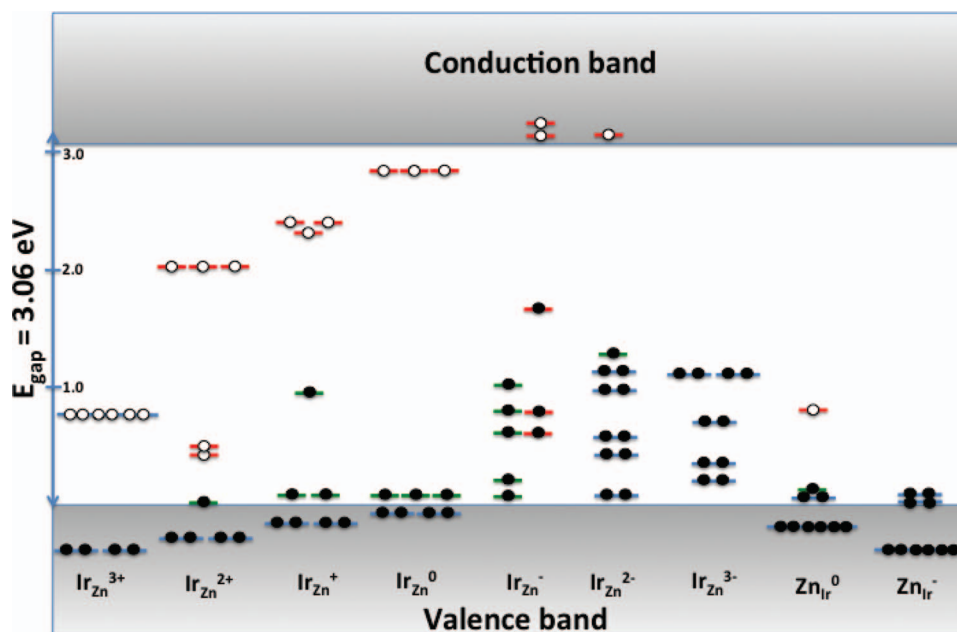

FIG. 7. Diagram representing the gap region of $ZnIr_2O_4$ with the localized states induced by antisite defects at different charge states. Ir_{Zn} refers to the Ir antisite and Zn_{Ir} refers to the Zn antisite. Filled circles represent electrons and open circles represent holes. Levels occupied with only one electron or hole are represented with green lines (spin-up) or red lines (spin-down).

levels from the NN Ir atoms are located at about 0.3 eV below the VBM. Addition of one electron to the cell reduces the three Zn-O elongated bonds from the neutral configuration to a bond length similar to that of the perfect structure. The deep unoccupied level of the neutral defect is now occupied and drops to 0.1 eV above the VBM. Additional electrons introduced in the model directly go into the conduction band.

C. Ir vacancy

Formation of a neutral Ir vacancy produces a localized hole on three NN O atoms. These atoms displace away from the vacancy by about 0.2 Å, while the other three O atoms surrounding the vacancy move away by about 0.1 Å. When more electrons are added to the supercell, each one of them eliminates a hole in a NN O atom and displaces the atom towards the vacancy by about 0.1 Å. When all holes have been eliminated, all NN O atoms are at the same distance from the vacancy.

As seen in Figure 6, the neutral vacancy creates a doubly occupied level and a single spin-up level resonant with the valence band, a doubly occupied and a spin-up singly occupied level at about 0.3-0.5 eV above the VBM and three unoccupied levels at about 0.9 eV and 1.1 eV above the VBM. Successive occupation of the unoccupied levels by the addition of up to three electrons to the supercell pushes the previously unoccupied levels to lower energies and increases the energy of the resonant states in the valence band, until a large group of levels close in energy is formed in the case of the defect with charge −3.

D. Ir antisite

Substitution of one Zn site for Ir produces only small perturbations in the local environment. The Ir atom maintains the fourfold coordination of the substituted Zn position, and the Ir–O bond lengths increase by about 0.1 Å due to the larger radius of the Ir atom. The tetragonal coordination modifies the d-d splitting of the Ir ion and creates three almost degenerate spin-up occupied levels near the VBM and three unoccupied levels near the CBM (see Figure 7). The three unpaired electrons are localized on the Ir antisite. Two doubly occupied resonant states are also created below the VBM. We calculated six charged states of the Ir antisite, from +3 to −3. Addition of electrons to the neutral cell gradually fills the vacant d orbitals of the Ir antisite and increases its distance to two of the four NN O atoms, breaking the tetrahedral symmetry in the process, until reaching about 0.3 Å in the case of the −3 charge state; it also lowers the energy of the unoccupied states to positions within 1–1.5 eV from the VBM and raises the energy of the resonant states until they enter the gap region around 0.5 eV above the VBM. On the other hand, addition of holes gradually empties the occupied d states of the antisite. It also reduces the distance between the NN O atoms and the Ir antisite by about 0.1 Å approximately keeping the tetrahedral symmetry. The unoccupied spin-up states increase their energy to about 0.5–1 eV above the VBM; the unoccupied spin-down states decrease their energy by about 0.5 eV.

When the +3 charge state is reached, all unoccupied states are located at about 0.8 eV above the VBM and the resonant valence band states are pushed 0.5 eV down into the valence band.

E. Oxygen vacancy

The neutral oxygen vacancy induces a displacement of the NN Zn atom of about 0.3 Å towards the cavity of the missing oxygen. The NN Ir positions are displaced by less than 0.1 Å from their original positions. Addition of a positive charge displaces the NN Zn atom back in the direction of its original position by about 0.2 Å. Finally the doubly positive vacancy induces the return of the NN Zn atom to approximately its original position. The NN Ir positions remain largely unaffected by the presence of the vacancy.

Figure 6 shows the positions of the defect levels induced by the oxygen vacancy with the three charge states. The neutral vacancy induces a doubly occupied level very close to the VBM, composed mostly from contributions of the d orbitals of the NN Ir atoms. This level is too far away from the CBM, so it cannot act as a donor in $ZnIr_2O_4$. Two degenerate levels are also induced inside the conduction band, close to the CBM. Progressive removal of charge from the defect induces the lifting of the now unoccupied levels from their original position near the VBM to the gap region of $ZnIr_2O_4$; one spin-down level in the case of the defect with charge +1, located at 1.3 eV above VBM, and one doubly unoccupied level in the case of the +2 charge state at 0.5 eV above the VBM. The levels previously located inside the conduction band go to lower energies in the gap region.

VI. AMORPHOUS $ZnIr_2O_4$

Once we have established the relationship between the presence of defects in the lattice and the electronic structure of $ZnIr_2O_4$, we proceed to study the amorphous phase using the melt-quench procedure described previously. We obtain a homogeneous amorphous phase for $ZnIr_2O_4$, whose volume is a 4.3% smaller than that of the crystalline phase. Figure 8 shows the partial radial distribution functions (rdf) of this structure. In general, the highest peaks in the rdf's are displaced towards shorter distances than in the spinel structure. In the case of the anion-cation distances and the Zn-Zn distance, the difference is of about 0.2 Å. In the Ir-Ir and Ir-Zn cases, distances are between 0.5 Å and 0.8 Å shorter than in the spinel.

We calculated average coordinations for cations and anions from the information contained in the rdf. In the Zn-O case, the average coordination value is similar to the crystal value. The Ir-O case is more remarkable, as the coordination drops from 6 in the crystal to about 5 in the amorphous phase. O atoms are coordinated on average to 1.2 Zn atoms (1 in the crystal phase) and 2.6 Ir atoms (3 in the crystal phase). These structural data indicate that the amorphous phase consists mainly of ZnO_4 and IrO_5 polyhedra. Like in the spinel phase, ZnO_4 units are largely isolated from each other. A significant amount of the IrO_5 polyhedra are linked to each other through their corners, while in the crystal phase all the IrO_6
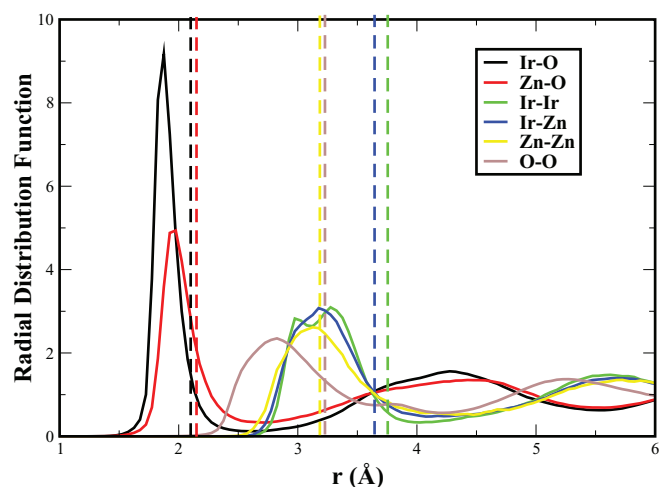
FIG. 8. Partial radial distribution functions of amorphous $ZnIr_2O_4$ generated from the melt-quench procedure. The dashed lines correspond to atom-atom distances in the spinel phase.

FIG. 9. Total DOS of amorphous and crystalline $ZnIr_2O_4$. The corresponding densities of states have been aligned with respect to the O 1s core level. The zero energy point has been arbitrarily chosen as the VBM in the spinel phase. The dashed vertical line shows the Fermi level of the amorphous phase.

octahedra are linked through their edges. These structural differences between crystal and amorphous phase may have a noticeable impact in the transparency of the system; it has been shown in Sec. V that changes in O or Ir coordination, induced by the creation of a defect in the lattice lead, in most cases, to the appearance of several states in the gap of the spinel phase. For example, the accommodation of the Ir atom into a fourfold-coordinated tetrahedral environment (the case of the Ir antisite) leads to the appearance of localized states near the band edges. Therefore, the generalized reduction of the coordination number and changes in polyhedra connectivity observed in the MD model may decrease the value of the band gap and lead to reduced transparency.

To test this hypothesis, we use the Reverse Monte Carlo method to construct a representative 91-atom model from the large MD supercell. We optimize its geometry using the B3LYP functional and analyze the resulting electronic structure. The amorphous model is 0.41 eV/atom higher in energy than the spinel phase. The DOS is shown in Figure 9. The most striking feature is the large reduction of the band gap with respect to the spinel structure, from 3.06 eV to about 1.2 eV. This reduction is caused by the presence of states at the band edges spanned by both undercoordinated Ir and O atoms and by sixfold-coordinated Ir atoms whose octahedral environment is heavily distorted. The presence of narrow localized states near the VBM makes them likely to play a significant role in polaron trapping processes and will severely affect the capability of amorphous $ZnIr_2O_4$ to act as a good hole conductor.

VII. DISCUSSION

Our results regarding formation energies and electronic structure of the different defects in $ZnIr_2O_4$ allow us to analyze their influence on the properties of technological interest for this material. One may notice from the electronic structure diagrams in Figures 6 and 7 that both cation antisites and vacancies induce unoccupied states in the gap region within 1 eV from the VBM. These levels may be
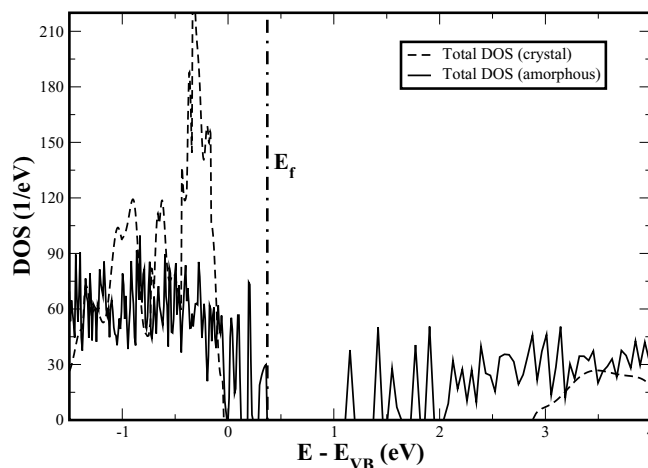
involved in optical absorption processes from the valence band with energies in the visible spectrum. Therefore, they may reduce the transparency of the spinel. These defects may also be active in the electrical properties of the material. Table II shows the defect transition levels for the cation vacancies and antisites. These defects have acceptor levels within 0.6 eV from the VBM which may contribute to p-doping in the spinel. The Ir antisite also induces several donor levels in the gap, but they are too deep to lead to a measurable concentration of free electrons.

Our calculations for the amorphous phase of $ZnIr_2O_4$ reveal a degradation of its transparency and hole conductivity induced by the presence of undercoordinated atoms and distorted IrO_x units. Additional insight into the changes in electronic structure induced by the amorphization process may be obtained by comparing amorphous $ZnIrO_4$ with amorphous pure or doped ZnO phases used in n-type conductivity applications. Examples of dopants include In, Ga, and Sn. In these cases, amorphization has only a minor impact on the band gap or the electronic conductivity of the system.[41] This is due to the isotropic nature of the cation s orbitals that form the CBM and permit them to conserve orbital overlap despite the disorder in the lattice. Some studies have suggested that this behaviour could be replicated in the valence band by considering the ZnM_2O_4 spinels with M=Co,Rh,Ir[8,42] due to the

TABLE II. Defect transition levels, in eV, for the cation vacancies and antisites in $ZnIr_2O_4$.

Defect	Transition (q/q′)	ϵ (q/q′)
V_{Ir}	(0/−2)	0.15
V_{Zn}	(0/−1)	0.53
	(−1/−2)	2.13
Ir_{Zn}	(−1/0)	0.60
	(0/−1)	1.54
	(−1/−3)	2.56
Zn_{Ir}	(0/−1)	0.40

more isotropic nature of the *d* orbitals forming the gap region compared with the O *p* orbitals. In the particular case of $ZnRh_2O_4$, these studies find that Rh-rich structures, in which edge-sharing RhO_6 octahedra predominate, have large band gap values (of the order of 2.1 eV). On the other hand, Rh-poor structures with corner-sharing RhO_6 octahedra have much smaller band gap values. Our calculations for amorphous $ZnIr_2O_4$ show that amorphization leads to a prevalence of corner-sharing IrO_x, which in turn leads to decreased values of the band gap with respect to the spinel phase. Moreover, amorphization also leads to the appearance of localized states at the VBM due to the presence of undercoordinated atoms and distorted IrO_6 octahedra, which means that the hole conduction mechanism is radically affected by the amorphization process. Summarizing, amorphization has a negative impact on both transparency and hole conduction. This result casts doubts about the general strategy of substituting O *p* orbitals at the top of the valence band with transition metal *d* orbitals to obtain good amorphous *p*-type transparent conducting oxides. A possible solution to the problem of localized states in the gap could be to incorporate dopants in the structure which would saturate the dangling bonds of the undercoordinated atoms that are present. This avenue will be explored in future studies.

VIII. CONCLUSIONS

We investigated the electronic structure and formation energy of different point defects in the spinel $ZnIr_2O_4$, and changes in the local geometry and electronic structure induced by amorphization of the material. Interstitial defects induce large distortions in the vicinity of the defect. The oxygen vacancy also distorts the lattice around the defect, although to a smaller degree than the interstitial defects. Cation vacancies and antisites produce only slight distortions in their closer neighbours. These findings result in larger formation energies for defects in the anion sublattice than for those in the cation sublattice, and very large formation energies for interstitial defects. The zinc antisite emerges from our results as the defect with the lowest formation energy, followed by the cation vacancies. It induces shallow acceptor levels, which may act as one of the possible sources for spontaneous hole doping in the material and as active defect in optical absorption that may reduce the transparency of $ZnIr_2O_4$. Amorphization of the material leads to a small decrease of the metal-oxygen distances and Zn-Zn distances, and to a large decrease of the Ir-Ir and Ir-Zn distances. The average Ir and O coordinations are also smaller, indicating the presence of a large amount of corner-linked IrO_5 polyhedra which lead to a smaller value of the band gap. The presence of localized states at the top of the valence band suggests the possibility of hole polaron trapping in the amorphous structure and low hole conductivities in the system.

ACKNOWLEDGMENTS

[1] H. Ohta, K.-H. Kawamura, M. Hirano, N. Sarukura, and H. Hosono, Appl. Phys. Lett. **77**, 475 (2000).

[2] G. Thomas, Nature **389**, 907 (1997).

[3] E. Fortunato, D. Ginley, H. Hosono, and D. C. Paine, MRS Bull. **32**, 242 (2007).

[4] A. Tsukazaki, A. Ohtomo, T. Onuma, M. Ohtani, T. Makino, M. Sumiya, K. Ohtani, S. F. Chichibu, S. Fuke, Y. Segawa *et al.*, Nat. Mater. **4**, 42 (2005).

[5] S. J. Jiao, Z. Z. ZHang, Y. M. Lu, D. Z. Shen, B. Yao, B. Zhang, H. Li, D. X. Zhao, X. W. Fan, and Z. K. Tang, Appl. phys. Lett. **88**, 031911 (2006).

[6] S. Narushima, H. Mizoguchi, K. Shimizu, K. Ueda, H. Ohta, M. Hirano, T. Kamiya, and H. Hosono, Adv. Mater. **15**, 1409 (2003).

[7] D. O. Scanlon, K. G. Godinho, B. J. Morgan, and G. W. Watson, J. Chem. Phys. **132**, 024707 (2010).

[8] T. Kamiya, S. Narushima, H. Mizoguchi, K. Shimizu, K. Ueda, H. Ohta, M. Hirano, and H. Hosono, Adv. Funct. Mater. **15**, 968 (2005).

[9] M. Dekkers, G. Rijnders, and D. H. A. Blank, Appl. Phys. Lett. **90**, 021903 (2007).

[10] J. Grochowski, E. Kaminska, A. Piotrowska, E. Dynowska, P. Dluzewski, J. Dyczewski, A. Szczepanska, and P. Kazmierczak, Phys. Status Solidi C **9**, 1504 (2012).

[11] T. R. Paudel, A. Zakutayev, S. Lany, M. d'Avezac, and A. Zunger, Adv. Funct. Mater. **21**, 4493 (2011).

[12] M. N. Amini, H. Dixit, R. Saniz, D. Lamoen, and B. Partoens, Phys. Chem. Chem. Phys. **16**, 2588 (2014).

[13] R. Dovesi, V. Saunders, C. Roetti, R. Orlando, C. M. Zicovich-Wilson, F. Pascale, B. Civalleri, K. Doll, N. M. Harrison, I. J. Bush *et al.*, *CRYSTAL09 User's Manual* (University of Torino, 2009).

[14] D. Muñoz Ramo and P. D. Bristowe, Thin Solid Films **555**, 112 (2014).

[15] C. H. Patterson, Phys. Rev. B **74**, 144432 (2006).

[16] F. Gallino, G. Pacchioni, and C. Di Valentin, J. Chem. Phys. **133**, 144512 (2010).

[17] D. Muñoz Ramo, A. Chroneos, M. J. D. Rushton, and P. D. Bristowe, Thin Solid Films **555**, 117 (2014).

[18] D. Muñoz Ramo, A. L. Shluger, J. L. Gavartin, and G. Bersuker, Phys. Rev. Lett. **99**, 155504 (2007).

[19] P. V. Sushko, S. Mukhopadhyay, A. S. Mysovsky, V. B. Sulimov, A. Taga, and A. L. Shluger, J. Phys.: Condens. Matter **17**, S2115 (2005).

[20] L. Giordano, P. V. Sushko, G. Pacchioni, and A. L. Shluger, Phys. Rev. Lett. **99**, 136801 (2007).

[21] F. Cora, M. Alfredsson, G. Mallia, D. S. Middlemiss, W. C. Mackrodt, R. Dovesi, and R. Orlando, Struct. Bond. **113**, 171 (2004).

[22] P. V. Sushko, A. L. Shluger, M. Hirano, and H. Hosono, J. Am. Chem. Soc. **129**, 942 (2007).

[23] N. Singh and U. Schwingenschlögl, Europhys. Lett. **104**, 37002 (2013).

[24] J. Paier, M. Marsman, and G. Kresse, J. Chem. Phys. **127**, 024103 (2007).

[25] E. A. Ahmad, L. Liborio, D. Kramer, G. Mallia, A. R. Kucemak, and N. M. Harrison, Phys. Rev. B **84**, 085137 (2011).

[26] S. Lany and A. Zunger, Phys. Rev. B **78**, 235104 (2008).

[27] G. Makov and M. C. Payne, Phys. Rev. B **51**, 4014 (1995).

[28] C. L. Bailey, L. Liborio, G. Mallia, S. Tomić, and N. M. Harrison, J. Phys. Conf. Ser. **242**, 012004 (2010).

[29] G.-M. Rignanese, J. Phys.: Condens. Matter **17**, R357 (2005).

[30] W. Smith and I. T. Todorov, Mol. Simul. **32**, 935 (2006).

[31] See supplementary material at http://dx.doi.org/10.1063/1.4893556 for further information about the calculation details and a description of the interstitial defects.

[32] R. L. McGreevy and L. Pusztai, Mol. Simul. **1**, 359 (1988).

[33] D. A. Keen and R. L. McGreevy, Nature **344**, 423 (1990).

[34] O. Gereben, P. Jovari, L. Temleitner, and L. Pusztai, J. Optoelectron. Adv. Mater. **9**, 3021 (2007).

[35] D. O. Scanlon and G. W. Watson, Phys. Chem. Chem. Phys. **13**, 9667 (2011).

[36]H. S. O'Neill and J. Nell, Geochim. Cosmochim. Acta **61**, 5279 (1997).

[37]J. A. Dean, *Lange's Handbook of Chemistry*, 14th ed. (McGraw-Hill, New York, 1992).

[38]M.-S. Miao and R. Seshadri, J. Phys.: Condens. Matter **24**, 215503 (2012).

[39]J. P. Perdew, K. Burke, and M. Ernzerhof, Phys. Rev. Lett. **77**, 3865 (1996).

[40]K. Reuter and M. Scheffler, Phys. Rev. B **65**, 035406 (2001).

[41]A. Walsh, J. L. F. Da Silva, and S.-H. Wei, J. Phys.: Condens. Matter **23**, 334210 (2011).

[42]H. Mizoguchi, M. Hirano, S. Fujitsu, T. Tomonari, K. Ueda, and H. Hosono, Appl. Phys. Lett. **80**, 1207 (2002).